APPLIED SCIENCES AND ENGINEERING

Magnetic field–enhanced vertical integration enables embodied intelligence in untethered soft robots

Xiaosa Li[1]†, Xiao Xiao[1]†, Xiao Xiao[2,3]†, Zixiao Liu[4], Junhao Gong[1], Zenan Lin[1], Bing Xue[5,6], Shibo Liu[7], Xinru Wu[1], Wei Zhang[5,6], Dongkai Wang[1], Runze Zhao[1], Zihan Wang[1], Xiongwei Zhong[1], Yiliang Lin[8], Patrick Chia[2], Ximin He[4], John S. Ho[2,6,9], Ghim Wei Ho[2,5], Wei Ouyang[7], Wenbo Ding[1]*, Guangmin Zhou[1]*, Cecilia Laschi[10,11], Changsheng Wu[2,3,5,6,9]*

Embodied intelligence in soft robotics offers unprecedented capabilities for operating in uncertain, confined, and fragile environments that challenge conventional technologies. However, achieving true embodied intelligence—which requires continuous environmental sensing, real-time control, and autonomous decision-making—faces challenges in energy management and system integration. We developed deformation-resilient flexible batteries with enhanced performance under magnetic fields inherently present in magnetically actuated soft robots, with capacity retention after 200 cycles improved from 31.3 to 57.3%. These compliant batteries enable large-area deployment of 44.9% across the robot body, and their vertical integration with rationally designed flexible hybrid circuits minimizes additional stiffness while maintaining deformability. This actuator-battery-sensor vertical integration methodology maximizes functional area utilization in a manta ray–inspired soft robot, establishing an untethered platform with sensing, communication, and stable power supply. The system demonstrates embodied intelligence in aquatic environments through diverse capabilities including perturbation correction, obstacle avoidance, and temperature monitoring, with proprioceptive and environmental sensing enabling real-time decision-making during magnetically actuated locomotion.

INTRODUCTION

Soft-bodied animals—from the waving octopus and drifting jellyfish to the gliding manta ray—demonstrate environment-adaptive movements through seamless vertical integration of locomotion, perception, and energy supply systems within their tissues (*1*). This natural architecture, where receptors, fat cells, and muscles are efficiently stacked, achieves a synergy that enables biological embodied intelligence (*2*, *3*). In contrast, conventional soft robots typically rely on lateral integration of functional modules—sensory, actuation, and energy units—to accomplish specific tasks (Fig. 1A). However, the limited structural space and inherent deformation of soft robots challenge the integration of energy-dense onboard power sources necessary for both sensing and communication (*4*). The lack of integrated power sources limits soft robots' ability to sustain operations and adapt dynamically, undermining their potential for true embodied intelligence (*5*, *6*).

The integration of energy-dense power sources into soft robots faces multiple challenges: structural constraints (*7*), operational stability (*8*), and mechanical compatibility (*9*). While recent advancements have demonstrated the feasibility of embedding chemical and electrical energy sources within the robots' mechanical framework (*10*–*12*), the continuous deformation and vibration inherent to soft robotics severely affect the electrochemical processes of onboard flexible batteries. These mechanical disturbances disrupt ionic deposition on the anode and intercalation/deintercalation on the cathode, leading to rapid capacity decay and short circuit risks (*13*, *14*). In addition, the modulus mismatch between gel electrolyte-based flexible batteries, electronic circuits, and robot actuators compromises movement capabilities (*15*). Thus, vertical integration is essential for enabling embodied intelligence in soft robots by maximizing functional area utilization, preserving mechanical compliance, and achieving seamless synergy among actuation, sensing, and energy systems.

We present a vertical integration methodology that leverages magnetic fields for dual purposes: enhancing battery performance and enabling robot control. Our approach demonstrates flexible battery design, multimodule synergy, and in situ somatosensory capabilities in a magnetically actuated manta ray soft robot. The design vertically integrates magnetic elastomer actuators, tandem flexible Zn-MnO_2 batteries, and flexible hybrid circuits, achieving biological-like synergy of locomotion, energy supply, and perception (Fig. 1B). The tandem flexible Zn-MnO_2 batteries, covering 44.9% of the robot's main body, serve as an energy-dense power source. Notably, the magnetic field from the magnetic elastomer actuator substantially improves the batteries' electrochemical processes under mechanical deformations, substantially suppressing cathode structure deterioration and anode dendrite growth (Fig. 1C). This enhancement enables improved capacity retention of flexible batteries from 31.3 to 57.3% after 200 cycles (Fig. 1D), achieving the benefits of magneto-electrochemistry in a fully flexible format. The flexible batteries, together with optimized

[1]Tsinghua Shenzhen International Graduate School, Tsinghua University, Shenzhen 518055, P. R. China. [2]Department of Electrical and Computer Engineering, National University of Singapore, Singapore 117583, Singapore. [3]SIA-NUS Digital Aviation Corporate Laboratory, National University of Singapore, Singapore 117602, Singapore. [4]Department of Materials Science and Engineering, University of California, Los Angeles, Los Angeles, CA 90095, USA. [5]Department of Materials Science and Engineering, National University of Singapore, Singapore 117575, Singapore. [6]Institute for Health Innovation and Technology, National University of Singapore, Singapore 117599, Singapore. [7]Thayer School of Engineering, Dartmouth College, Hanover, NH 03755, USA. [8]Department of Chemical and Biomolecular Engineering, National University of Singapore, Singapore 117585, Singapore. [9]The N.1 Institute for Health, National University of Singapore, Singapore 117456, Singapore. [10]Department of Mechanical Engineering, National University of Singapore, Singapore 117575, Singapore. [11]Advanced Robotics Centre, National University of Singapore, Singapore 117575, Singapore.
*Corresponding author. Email: ding.wenbo@sz.tsinghua.edu.cn (W.D.); guangminzhou@sz.tsinghua.edu.cn (G.Z.); cwu@nus.edu.sg (C.W.)
†These authors contributed equally to this work.

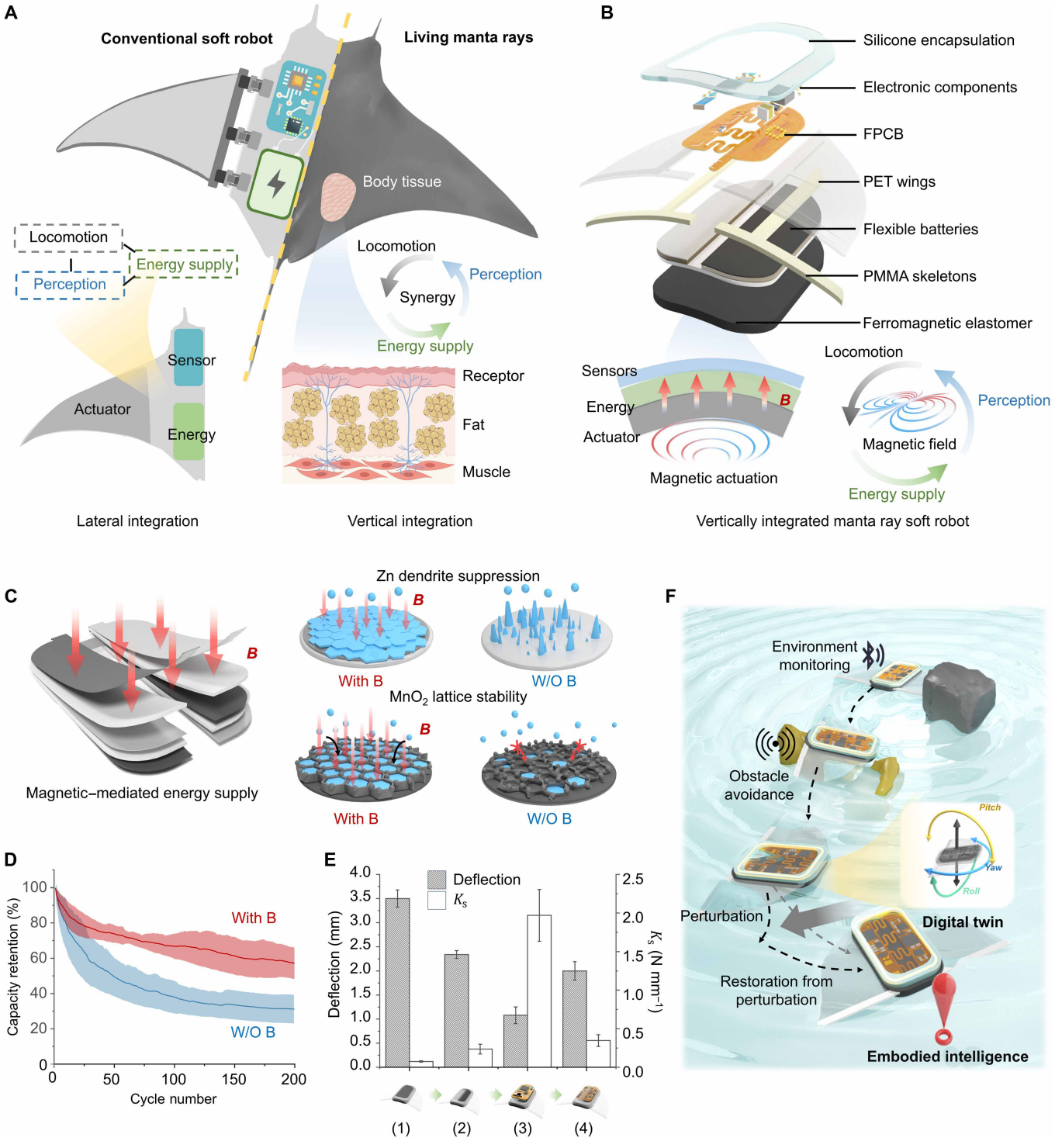

Fig. 1. Magnetic field–enhanced vertical integration enables embodied intelligence in untethered soft robots. (**A**) Comparison between biological embodied intelligence, achieved through vertical integration of receptors, fat cells, and muscles, and conventional soft robots' lateral integration of functional modules (sensory, actuation, and energy units). (**B**) Schematic of the manta ray–inspired soft robot demonstrating vertical integration of magnetic elastomer actuators, flexible Zn-MnO_2 batteries, and flexible hybrid circuits for synergistic locomotion, energy supply, and sensing. (**C**) Mechanism of magneto-electrochemical enhancement: the magnetic field from ferromagnetic elastomer suppresses both Zn dendrite growth and MnO_2 cathode deterioration in onboard battery. (**D**) Comparative capacity retention of flexible Zn-MnO_2 batteries after 200 cycles with and without magnetic field. The error bar indicates the SDs from the data of five independent samples. (**E**) Comparison of wing tip deflection and deformation stiffness (K_s) under applied manipulation magnetic fields across integration stages: (1) unloaded robot, (2) with flexible batteries, (3) with unoptimized circuit board, and (4) with optimized flexible hybrid circuit. The error bar indicates the SDs from the data of five independent samples. (**F**) Demonstration of embodied intelligence through digital twin–enabled obstacle avoidance and perturbation correction.

flexible hybrid circuits, enable compliance, embodied intelligence, and maximal functional area utilization in the manta ray soft robot. Within operational magnetic field strengths, this vertical integration endows the robot a bending stiffness of 0.348 N mm^{-1}, preserving the essential compliance of the soft actuator (Fig. 1E). The integrated sensing and communication modules provide real-time six-axis inertial data and temperature data, enabling digital twins for autonomous obstacle avoidance, perturbation correction, and environmental monitoring, enhancing the robot's adaptability in complex environments (Fig. 1F).

RESULTS

Magnetic field–enhanced Zn-MnO_2 batteries

Untethered soft robots, capable of programmable shape transformation and locomotion in response to various stimuli, rely critically on actuation systems (*16*). Among available control methods, magnetic fields offer unique advantages for precise remote manipulation in enclosed spaces (*17*), enabling applications ranging from biomedical interventions (*18*–*20*) to environmental monitoring (*21*, *22*). Magnetic fields also substantially influence electrochemical processes through magneto-electrochemistry, regulating mass transport (*23*, *24*) and charge transfer (*25*, *26*) kinetics in battery systems. In our vertical integration strategy, we exploit this dual functionality by using magnetic elastomer actuators that simultaneously enable robot manipulation and enhance battery performance through their generated magnetic fields. For our untethered soft robot operated in a water environment, we select flexible Zn-MnO_2 batteries as the power source for its decent volumetric capacity (*27*), safety (*28*), low cost (*29*), and water-proof capability (*30*). To validate this approach, we first investigated magneto-electrochemical effects on Zn-MnO_2 batteries (fabrication details presented in Materials and Methods) using a modified coin cell design where a permanent plate magnet serves as the gasket, generating a magnetic flux density $|B| \sim 93$ mT (detailed in fig. S1).

The magnetic field modulates the electrochemical process through the Lorentz force ($F_L = j \times B$), acting perpendicular to both current density (j) and magnetic field (B). Owing to irregularities at the electrode surface, such as protrusions and roughness, the nonuniform current density induces magnetohydrodynamic effects that fundamentally alter ion transport. Microscopically, ions undergo spiral trajectories around magnetic flux line, with orbit radii determined by $r = mv_\perp/qB$, where m is ion mass, $v_\perp$ is velocity perpendicular to the magnetic field, and q is the ion charge. This spiral motion selectively suppresses horizontal electromigration of Zn^{2+} ions—a primary cause of dendrite formation—while maintaining vertical transport along the magnetic field direction. The resulting reduction in perpendicular diffusivity, coupled with preserved axial diffusion, promotes uniform ion distribution across the electrode surface and alleviates concentration polarization (*31*, *32*). By reducing localized ion accumulation at surface irregularities, this magnetic field–induced microspiral motion enables homogeneous Zn^{2+} deposition and dendrite-suppressed electrochemical processes.

Finite element analysis demonstrates how these effects suppress dendrite formation (Fig. 2A and fig. S2; details are presented in Materials and Methods). Galvanostatic charge-discharge (GCD) tests on Zn||Zn symmetric electrodes confirm enhanced stability under a magnetic field (Fig. 2B). The magnetic field substantially extends cell life span from 197, 316, 543, and 776 hours to 294, 493, 873, and 1303 hours at 20, 10, 5, and 2 mA cm^{-2}, respectively (Fig. 2C and fig. S3). Zn anodes under a magnetic field exhibit ~60% longer life span and ~30% smaller voltage hysteresis. Scanning electron microscopy and x-ray diffraction of Zn anodes after 300 cycles at 5 mA cm^{-2} reveals that magnetic field promotes uniform Zn deposition with preferred (002) plane orientation, suppressing dendrite formation, in contrast to irregular deposition and dendrite formation in unenhanced samples (Fig. 2D and fig. S4). Cross-sectional analysis exhibit reduction in deposition thickness under a magnetic field and much less Zn dendrites growth across different current densities (fig. S5). We further validate the benefits of magnetic field in improving homogeneous Zn deposition in Zn-MnO_2 coin cells by Tafel plots (fig. S6) and self-discharge tests (fig. S7).

Beyond improved ion transport and deposition on Zn anode, the magnetic field also stabilizes MnO_2 lattice via spin-aligned electronic interactions between magnetic field and electrons of Mn species (*33*). Specifically, the external magnetic field aligns electron spin states in Mn-O bonds, strengthening Mn^{3+}-O bonds and reducing crystal distortions and Mn dissolution. Rate performance tests across three periods of 10 charging-discharging cycles each (0.2, 0.5, 1.0, 2.0, and 5.0 C) show that magnetically enhanced Zn-MnO_2 cells maintain 94.2 and 88.1% of initial capacity in the second and third periods, compared to 86.3 and 75.6% without enhancement (Fig. 2E). Galvanostatic intermittent titration technique (GITT) measurements reveal average Zn^{2+} diffusion coefficients ($D_{Zn^{2+}}$) of 3.28×10^{-8} and 2.86×10^{-8} cm^2 s^{-1} for charging and discharging under magnetic fields, respectively, ~38.4% higher than unenhanced samples (Fig. 2F). To understand MnO_2 cathode stability during Zn^{2+} intercalation and redox reactions, we characterized the structural evolution using multiple techniques. X-ray photoelectron spectroscopy and Raman spectroscopy reveal valence state changes and chemical bonding variations during cycling (figs. S8 and S9), while in situ synchrotron x-ray diffraction tracks lattice evolution (fig. S10). High-resolution transmission electron microscopy (HRTEM) demonstrates preserved octahedral [MnO_6] structure with ordered hexagon patterns after 1000 cycles at 0.2 A g^{-1} under a magnetic field, contrasting with lattice spacing distortions in unenhanced samples (Fig. 2, G and H). This structural stability enables 87.8% capacity retention over 2000 cycles, compared to 76.7% without magnetic enhancement (Fig. 2I). Density functional theory calculations reveal that magnetic fields strengthen Mn-O bonding through enhanced Mn-3d and O-2p orbital overlap in the Mn^{4+}/Mn^{3+} redox couple, improving resistance to stress-induced deterioration and Jahn-Teller effects (fig. S11). The projected density of states (PDOS) analysis based on density functional theory calculations (Fig. 2J) shows enhanced overlap between Mn-3d and O-2p orbitals in the Mn^{4+}/Mn^{3+} redox couple under a magnetic field, leading to more robust 3d-2p hybrid orbital formation. This spin-aligned state stabilizes the Mn oxidation environment, suppressing the accumulation of isolated Mn^{3+} species that are prone to disproportionation into soluble Mn^{2+}. Therefore, the strengthened M-O bonding stabilizes the MnO_2 cathode structure against deterioration mechanisms, including irregular stress concentrations (*34*) and Jahn-Teller distortions (*35*, *36*), explaining the improved long-term capacity retention.

Magnetic field–enhanced vertical integration in a manta ray soft robot

To demonstrate the utility of magneto-electrochemical enhancement in Zn-MnO_2 batteries in soft robotic applications, we developed a vertically integrated manta ray–inspired ferromagnetic soft

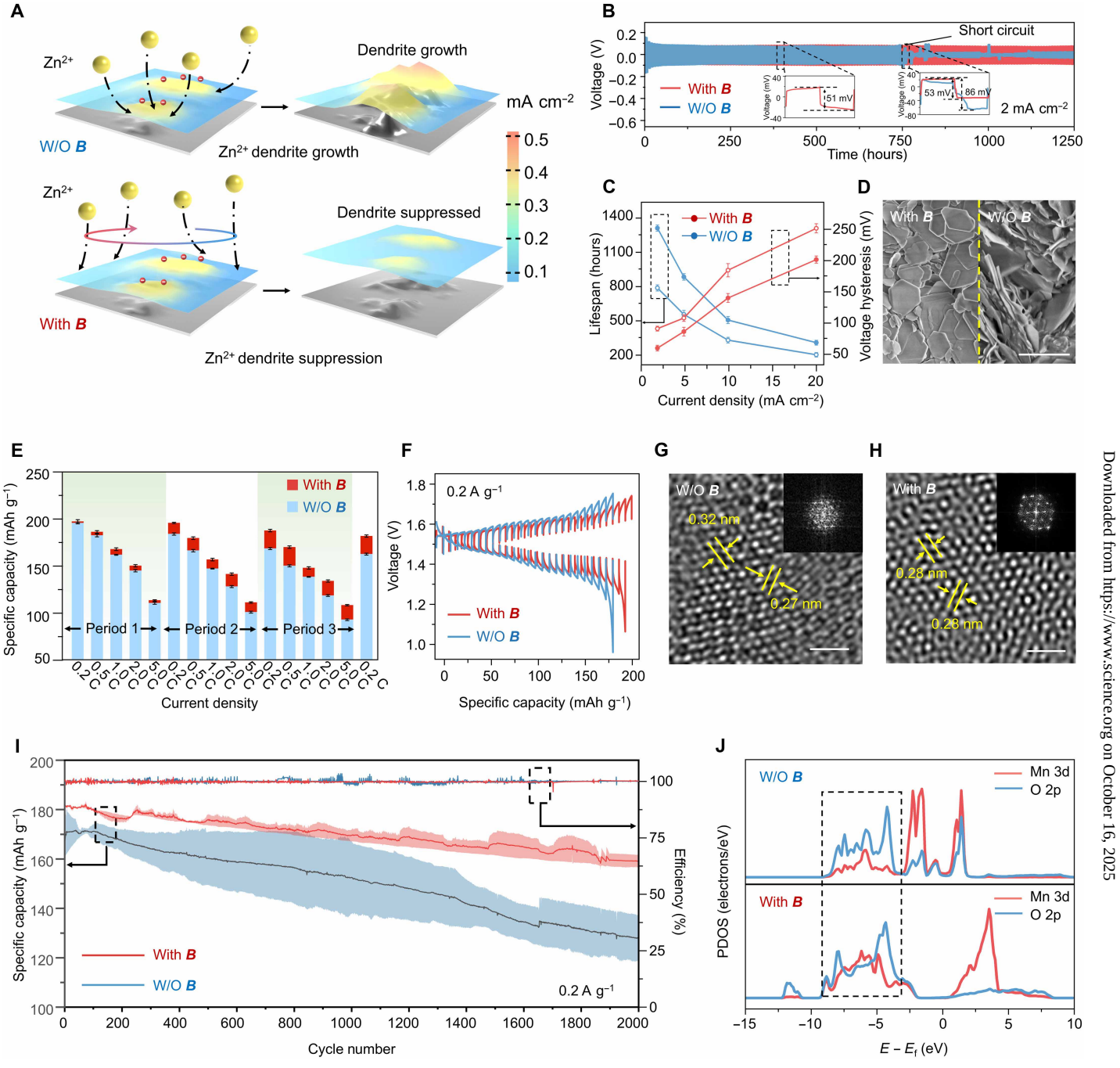

Fig. 2. Magneto-electrochemical enhancement mechanism and characterization in Zn||Zn symmetric coin cells and Zn-MnO_2 coin cells. (**A**) Illustrative comparison of Zn dendrite growth patterns with and without applied magnetic field. (**B**) GCD profiles of Zn||Zn symmetric coin cells at 2 mA cm^{-2} under magnetic field influence. (**C**) Comparative analysis of life span and voltage hysteresis in Zn||Zn symmetric coin cells across different current densities, with and without magnetic field. The error bar indicates the SDs from the data of three samples. (**D**) SEM visualization of Zn electrode surface morphology after 300 cycles (scale bar, 10 μm). (**E**) Comparison of the average capacity of Zn-MnO_2 coin cells cycled at 0.2, 0.5, 1.0, 2.0, and 5.0 C across three test periods with and without magnetic field. The error bar indicates the SDs from the capacity data of five cycles. (**F**) GITT analysis after rate performance testing, comparing diffusion kinetics with and without magnetic field. (**G** and **H**) HRTEM lattice fringe images of MnO_2 cathode structure after 1000 cycles without (G) and with (H) magnetic field (scale bar, 1 nm). (**I**) Extended cycling performance comparison of Zn-MnO_2 coin cells under magnetic field influence. The thick solid lines and shaded bands indicate the means and SDs from the data of 5 samples. (**J**) Projected density of states (PDOS) analysis showing Mn 2p and O 2p orbital overlap in MnO_2 lattice under a magnetic field.

robot (fig. S12) that exploits magnetic fields for dual functionality. The manta ray–like geometry offers the structural foundation for our aquatic soft robot, and the design vertically stacks flexible Zn-MnO_2 batteries (fig. S13) onto a ferromagnetic elastomer actuator with NdFeB microparticles (~5 μm) uniformly dispersed in a silicone matrix (details presented in Materials and Methods, fig. S14, and movie S1). This configuration generates magnetic fields that simultaneously enhance battery performance and enable untethered robotic control, maximizing functional area utilization while preserving mechanical compliance.

We implemented an orthogonal multiaxis magnetization strategy for the ferromagnetic actuator (Fig. 3A and fig. S15). The method combines axial and cosinusoidal magnetization patterns (fig. S16A). Axial magnetization along the *x* axis imparts directionality to the robot, causing it to align with the horizontal field direction under the influence of the magnetic torque τ_z (fig. S16B), and move along the field gradient. Cosinusoidal magnetization in the *yz* plane is symmetrical along the central *x* axis of the robot, allowing the robot to bend up-and-down under the torque τ_x actuation of the vertical field component (fig. S16C). Cosinusoidal magnetization facilitates the formation of the closed magnetic flux loop and can enable a high robot's magnetic field up to ~50 mT. As a result, the strong field of the ferromagnetic elastomer not only enhances the performance of the adjacent flexible battery, but also helps maintain the robot's deformability in vertically integrated configurations, ensuring its aquatic locomotion stability and adaptability (see text S1).

The vertical integration strategy ensures proximity between the flexible battery and the magnetic elastomer, substantially enhancing the stability of Zn-MnO_2 batteries (details in Materials and Methods) under various mechanical conditions. Cycling tests beyond 200 cycles demonstrated superior electrochemical performance when batteries were coupled with magnetized elastomer under continuous mechanical vibrations with a frequency of 30 Hz and an amplitude of 5 mm (Fig. 3B, experimental details in Materials and Methods). In addition, we evaluated the capacity retention of flexible Zn-MnO_2 batteries under varying bending angles and curvature radii. Under mechanical deformation, both bending angle and curvature radius substantially influence battery performance. As the bending angle increased from 0° (flat) to 135° (sharp bend), the average capacity retention of the magnetically enhanced batteries after 200 testing cycles dropped from 57.3% to 33.5%, while control samples exhibited a more severe decline from 31.3% to 10.2% (fig. S17). Similarly, as the curvature radius decreased from ∞ (flat) to 2 mm at a fixed bending angle of 90°, the magnetically enhanced batteries retained 57.3% to 46.7% of their capacity, whereas the control samples fell to 31.3% to 12.8%. These results highlight that our magnetic field–assisted integration strategy effectively mitigates deformation-induced capacity degradation, maintaining reliable energy output even under mechanically challenging conditions.

To achieve embodied intelligence while preserving mechanical compliance, we rationally designed a flexible hybrid circuit to achieve the robot's sensory and communication functionalities (fig. S18). We characterized the magnetic-induced deformation capability of the robots under the general actuation field strength (8 to 15 mT, detailed in fig. S19 and Materials and Methods). At a maximum field strength of 15 mT, measurements revealed that average wing tip deflections were 3.5 mm in unloaded robots and 2.0 mm in fully integrated robots (Fig. 3C). To characterize mechanical properties across integration stages, we conducted three-point bending tests to measure force-deflection relationships (experimental details presented in Materials and Methods and fig. S20). Analysis of deformation stiffness (K_s) characterized as secant slope from 0 to the maximum magnetic-induced deflection in fully integrated robots (2 mm) revealed that our strategy with optimized flexible hybrid circuit and flexible batteries preserved mechanical compliance (movie S2), with K_s increasing from 0.08 to 0.35 N mm^{-1}, in contrast to 1.97 N mm^{-1} of that with an unoptimized circuit board (Figs. 1E and 3D). Finite element analysis corroborated these findings, predicting wing tip deflections of 3.50, 2.04, and 1.03 mm for unloaded, optimized, and unoptimized designs, respectively (fig. S21). This close agreement between simulation and experimental results validated our optimization approach for maintaining compliance through vertical integration.

The integrated soft robot's magnetic elastomer enables its motion under the guidance of field generation devices, such as a mobile coil or an electromagnet array, while its onboard battery and circuit support the use of an inertial sensor to collect the robot's motion data, which is wirelessly transmitted to a host computer via Bluetooth low energy (BLE) as the feedback for actuation strategy adjustment. BLE communication and system temperature remain stable in magnetic fields (fig. S22), making it suitable for the magnetically actuated application. The block diagram of the closed-loop magnetically actuated soft robot system is shown in Fig. 3E. This untethered actuation system enables real-time information sharing of six-axis inertial data and task-oriented sensors, enhancing operational monitoring and actuation (movie S3). In a Unity 3D-powered virtual reality environment, the digital twin replicates the robot's real-time movements using processed six-axis inertial data. Figure 3F demonstrates precise synchronization between physical and digital representations (movie S4), laying a solid foundation for autonomous adaptation in complex environments.

Embodied intelligence in untethered soft robot

The untethered soft robot acquires its directionality under the axial magnetization, enabling the basic aquatic movements such as steering and displacement under the guidance of spatial magnetic fields (see text S2). Specifically, the robot tends to change its orientation and align with the horizontal field direction. Besides, the magnetic dipole formed at the head and tail of the robot due to axial magnetization can be captured by the field with the opposite dipole distribution generated by the coil system. The captured robot can follow the movement of the mobile coil's field, or move along the direction of the descending magnetic field gradient from adjacent coils, thereby achieving magnetically actuated displacement within a mobile coil or an electromagnet array (figs. S23 to S25). As shown in Fig. 4A, the automated magnetic actuation of the untethered soft robot was implemented using an electromagnetic coil and the dipole magnet mounted on the robotic arm. Efficient locomotion (three body lengths/1.8 s) in linear paths (movie S5) and agile trajectory movement through 90° turns (movie S6) and tee joints (movie S7) were executed via combined steering-displacement maneuvers.

Vertical integration of flexible battery and circuit on the soft robot enables both proprioceptive and environmental sensing. Such information is essential for supporting the robot's embodied intelligence to carry out exploration missions in confined and visionless settings. For instance, within pipelines and industrial reaction devices, the integrated robot can use its onboard temperature sensing to detect environmental temperature changes by an unknown heat source (fig. S26 and movie S8). Moreover, the robot actuation system

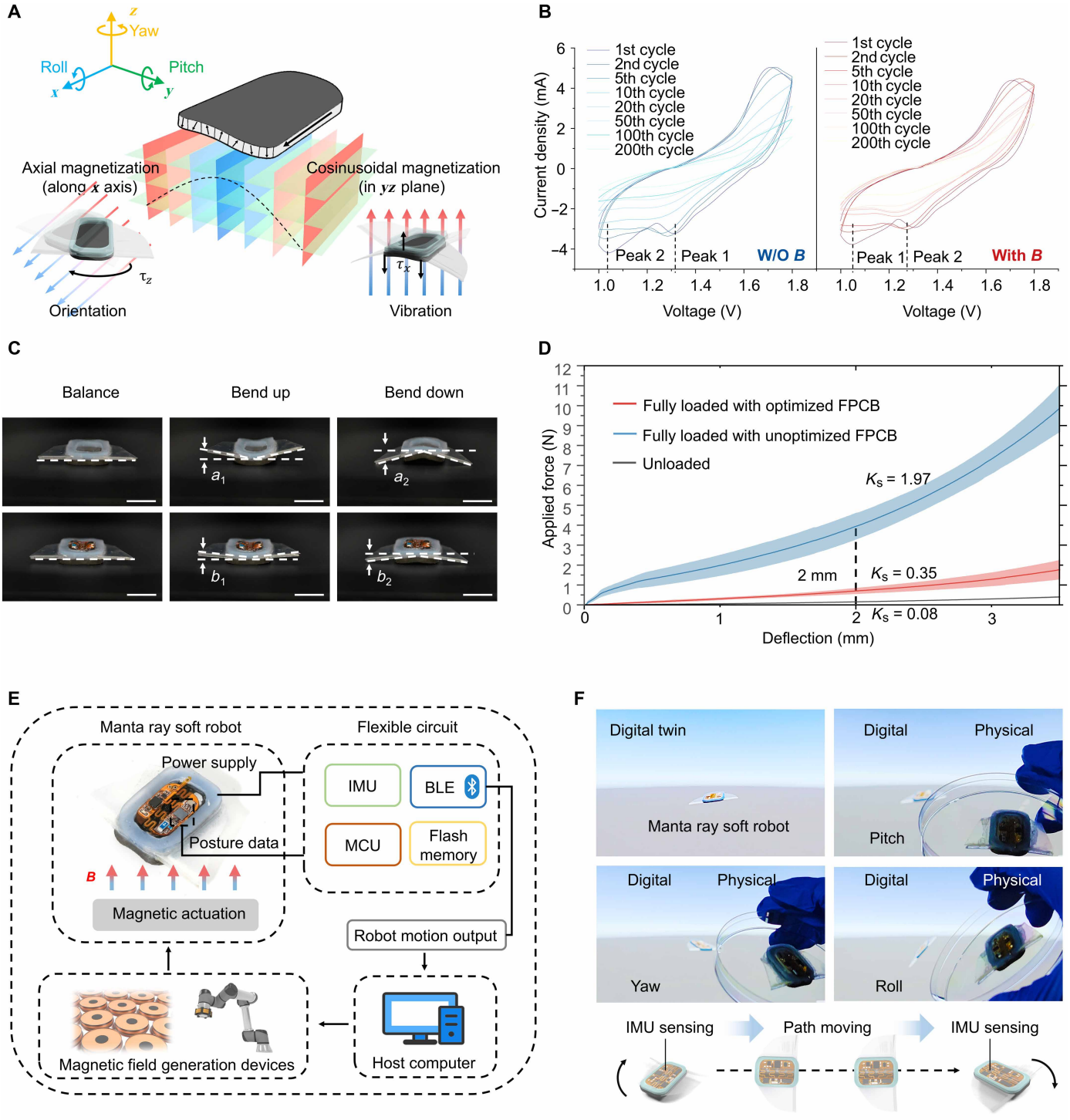

Fig. 3. Magnetic field–enhanced vertical integration for untethered soft robot design. (**A**) Orthogonal multiaxis magnetization of the manta ray soft robot: axial magnetization for steering and cosinusoidal magnetization for bending deformation. (**B**) CV analysis of flexible Zn-MnO_2 batteries under continuous vibration, comparing long-term cycling stability with and without magnetic field enhancement. (**C**) The average wing tip deflections of soft robots under a 15-mT magnetic field: unloaded $(a_1 + a_2)/2 = 3.5$ mm versus fully loaded $(b_1 + b_2)/2 = 2.0$ mm, 5 samples each. Scale bar, 1 cm. (**D**) Force-deflection curves of manta ray soft robots before and after vertical integration of flexible Zn-MnO_2 batteries and optimized flexible hybrid circuit. The thick solid lines and shaded bands indicate the means and SDs from the data from five samples. (**E**) The functional block diagram of the magnetic robot with magnetic actuation systems (the electromagnet array or mobile coil system). (**F**) Real-time digital twin visualization demonstrating precise posture replication and monitoring.

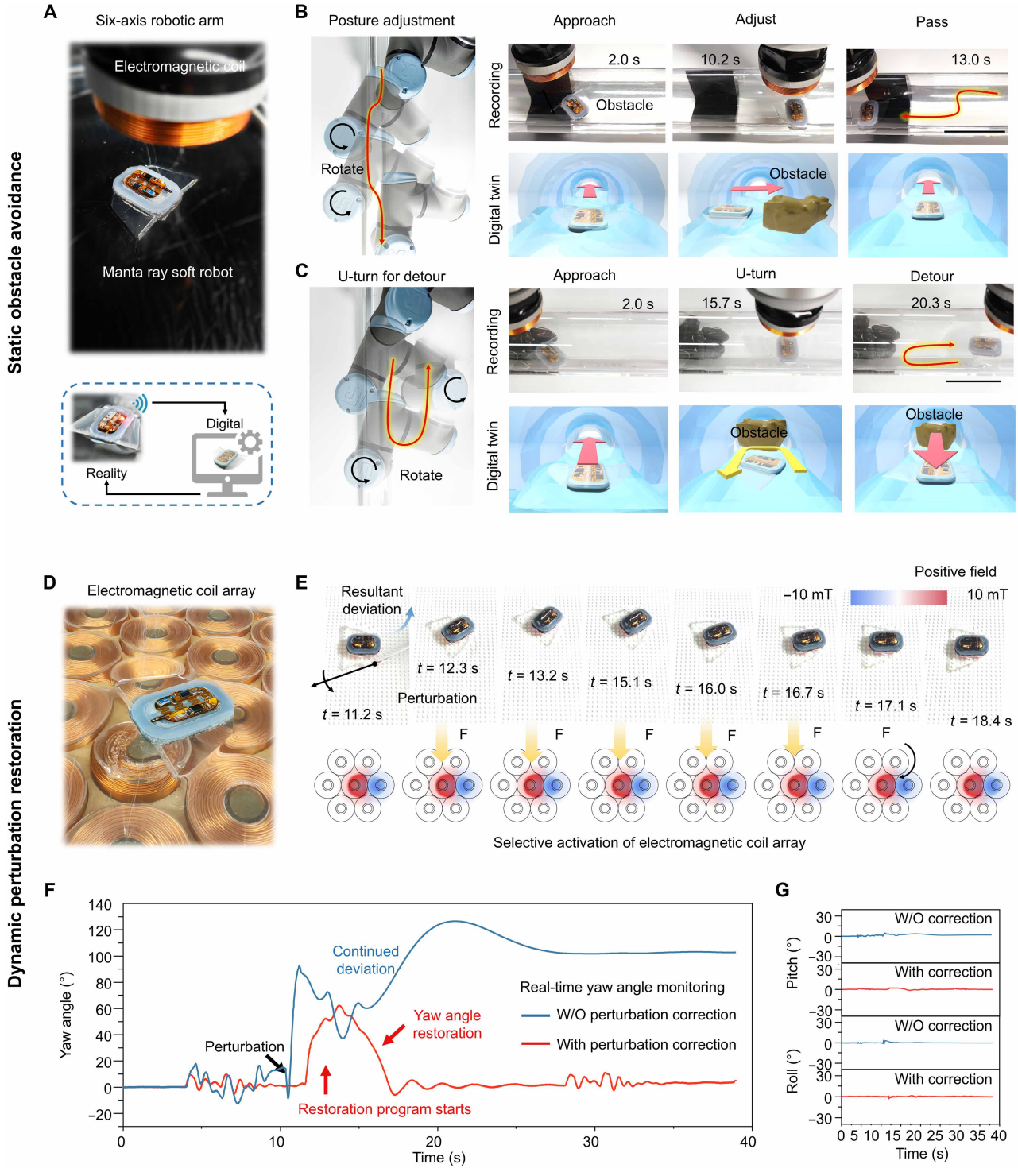

Fig. 4. Digital twin–enabled embodied intelligence for autonomous environmental exploration and perturbation correction. (**A**) Mobile coil system implementation for automated obstacle avoidance on water surface through real-time sensing (**B**) Digital twin visualization of autonomous narrow passage navigation, showing real-time posture adjustment capability. (**C**) Autonomous decision-making demonstration: digital twin recording of U-turn execution when encountering impassable obstacles. (**D**) Electromagnet array configuration for dynamic perturbation correction. (**E**) Position and orientation restoration following external disturbances using the perturbation correction program. (**F**) Comparative yaw angle analysis with and without perturbation correction program activation. (**G**) Pitch and roll angle stability maintenance during perturbation correction.

can use the sudden changes in the received inertial data (see Materials and Methods) to make real-time robot actuation adjustment. For example, during linear trajectory motion guided by the mobile coil, a noticeable fluctuation appears in the acceleration data of the *x* axis (robot heading axis) when the robot collides with a narrow passage or an obstacle (fig. S27). When a collision event is detected, the mobile coil system adjusts the robot's posture through the steering maneuver to navigate narrow passages (Fig. 4B and movie S9). The digital twin records both robot locomotion and obstacle locations. When encountering impassable obstacles after multiple avoidance attempts, the system initiates a U-turn protocol for backtracking, marking such routes with yellow U-turn arrows in the digital twin (Fig. 4C and movie S10).

Embodied intelligence in the untethered soft robot not only enables it to detect and maneuver around static obstacles, but also helps identify dynamic disturbances and make automatic corrections. When positioned above the electromagnet array, the robot is guided to perform the linear trajectory movement by sequentially activating the coils along the path. Using the delocalized magnetic actuation (fig. S28), the electromagnet array system achieves perturbation correction through programmed variations in local magnetic flux distribution. When disturbed by sudden external forces (e.g., glass rod), the soft robot deviates from its trajectory due to the interaction of the external force and the existing magnetic field. At this stage, the digital twin can detect fluctuations in the robot's acceleration and angular velocity, as well as the yaw angle error, and then notify the electromagnet array to initiate a position or orientation correction protocol (Fig. 4E and movies S11 and S12). Real-time yaw angle recordings demonstrate the effectiveness of this approach. During a 15-s interval, robots without the restoration program showed yaw angle deviations exceeding 90° after rod contact, with continued deterioration over time. In contrast, the robots with the restoration program showed accurate position and orientation restoration after yaw angle deviation (Fig. 4F). Besides, the perturbation correction program preserved the robot's pitch and roll angle stability, demonstrating robust posture actuation during dynamic perturbation recovery (Fig. 4G).

DISCUSSION

Our magnetically enhanced vertical integration strategy addresses fundamental challenges in achieving embodied intelligence for untethered soft robotics. Unlike previous approaches that focused on external feedback control or simple module stacking, our methodology demonstrates how magnetic fields can simultaneously enable actuation and enhance onboard power stability. The dual functionality of magnetic fields, combined with conformal vertical integration of actuator-battery-sensor modules, achieves true embodied intelligence while maximizing space utilization—critical for small-scale soft robots operating in constrained environments.

The demonstrated enhancement of flexible battery performance under magnetic fields provides insights for robust power system design in dynamic soft systems. Magnetic field stabilization of electrode processes, particularly in suppressing degradation under deformation, enables reliable power supply during robotic exploration. This stability allows the robot to perceive environmental conditions and intelligently respond to obstacles or disturbances through real-time sensing and closed-loop control.

The current system, equipped with inertial sensors and BLE communication, demonstrates basic embodied intelligence capabilities including temperature monitoring, collision detection, and autonomous navigation. The integration of advanced miniaturized sensors could further enhance task execution capabilities. Hall sensors could improve magnetic localization for autonomous navigation (*37*), while cameras or ultrasonic sensors could enhance the perception of unknown environments. Chemical sensors could monitor water quality, and specialized surface coatings could collect nanoplastic pollution (*38*). Our vertical integration platform provides a versatile foundation for such multimodal sensing while maintaining locomotion performance.

Although magnetic actuation provides extended operational endurance, battery capacity remains a limiting factor for autonomous tasks. The current system sustains approximately 2.3 to 3.8 hours of operation given an average battery capacity of ~3.8 mAh and a current consumption of 0.99 to 1.68 mA depending on operation modes (fig. S29). However, our demonstration that magnetic field enhancement is effective in lithium-ion batteries (fig. S30) suggests broader applicability across different battery chemistries, offering pathways to higher energy densities. Future integration of energy harvesting methods, such as magnetic resonance coupling, radio frequency, or biochemical energy harvesting, could enable energy replenishment during locomotion. These advances could unlock long-term autonomy for real-world applications while enabling more sophisticated sensing and control capabilities in soft robots.

MATERIALS AND METHODS

Fabrication and electrochemical characterization of modified Zn-MnO_2 coin cells

Modified Zn-MnO_2 coin cells were fabricated using CR2032 battery cases (diameter 20 mm, thickness 3.2 mm) with commercial Zn anode (0.3 mm, Qingyuan Sinogar Metal), electrolyte, and MnO_2 cathode. The electrolyte synthesis involved dissolving PVA powder [8.5 g, M_w (weight-average molecular weight) 146,000 to 186,000, Acros] in deionized water (100 ml) at 85°C, followed by dropwise addition of GO dispersion (1500 μl, 5 mg/ml, GaoXi Tech). The solution underwent freeze-thaw cycling (−6°C, 18 hours to room temperature, 1 hour) for enhanced cross-linking, followed by soaking in electrolyte (1.0 M $ZnSO_4$, 99.5%, Innochem, 0.3 M $MnSO_4$, 99.99%, Innochem) for 24 hours (*39*).

The MnO_2 cathode active material was synthesized by reacting $MnSO_4$ (0.755 g, 98%, Aladdin) and $K_2S_2O_8$ (1.35 g, 99%, Aladdin) in deionized water (100 ml) with dropwise addition of 1.2 M NaOH solution (25 ml, prepared using NaOH flakes, 96%, Innochem) under magnetic stirring, followed by 2 hours mixing and 1 hour aging. The MnO_2 powder was obtained by filtration rinse and vacuum freeze drying for 48 hours. The final MnO_2 cathode was prepared by coating a 7:2:1 slurry of MnO_2, conductive carbon (Ketjenblack ECP 600JD), and polyvinylidene fluoride (M_w ~275,000, Aladdin) onto an ethanol-rinsed carbon paper (TGP-H-060, TORAY INDUSTRIES Inc.).

For cell assembly in the CR2032 battery case, electrode and electrolyte components were cut into 19-mm-diameter discs. To investigate magnetic field effects, standard gaskets were replaced with NdFeB discs (18 mm diameter, 1 mm height) to generate a ~93-mT magnetic field within the cell. Rate performance was evaluated at

multiple C rates (0.2, 0.5, 1.0, 2.0, and 5.0 C), and long-term cycling stability was assessed at 0.2 A g^{-1} using NEWARE CT-4000 and Landt CT-2000 testing systems.

Finite element analysis of magnetohydrodynamic effects

Finite element simulations were performed using COMSOL Multiphysics to analyze magnetohydrodynamic effects on Zn^{2+} ion transport under applied magnetic field (100 mT) and electrical potential (1.4 V). The coupled electromagnetic and fluid dynamic behavior was modeled using electric currents and laminar flow interfaces to visualize ion transport trajectories.

Electrode material characterization

Crystal structures of battery electrodes were analyzed using powder x-ray diffraction (D8 advance, Bruker) with Cu-Kα radiation (λ = 1.54 Å). Surface morphology and corresponding energy-dispersive x-ray spectra (EDS) were characterized by field-emission scanning electron microscopy (MIRA3, TESCAM). Detailed structural analysis was performed using transmission electron microscopy (Tecnai F30, FEI) at 300 kV, while high-resolution dark-field imaging and EDS elemental mapping were conducted on a double Cs-corrector equipped microscope (Titan Themis G2 60-300, FEI) at 300 kV. Chemical bonding was investigated through Fourier transform infrared spectroscopy (Nicolet iS50, Thermo Electron), and valence bond information was analyzed by x-ray photoelectron spectroscopy (PHI5000VersaProbeII, Thermo Fisher Scientific).

Density functional theory calculations

First-principles calculations were performed using the Vienna Ab initio Simulation Package (VASP) (*40*). To take better account of electron correlations in 3d orbital of transition metal ions, we used the GGA + U approach (*41*) with Perdew-Burke-Ernzerhof functional (*42*) and the projected augmented wave method (*43*). The effective Hubbard parameters (U_{eff} = Coulomb U – exchange J) were set to 4 and 7 eV for Mn and Zn, respectively. The plane-wave cutoff energy was set to 400 eV. The Brillouin zone was sampled using the Monkhorst-Pack scheme with 5 × 5 × 2 k-point grids. To simulate the influence of the magnetic field on MnO_2 cathode, we used "LNONCOLLINEAR" and "SAXIS" keywords to make the spin of Mn elements to a specific direction (*44*). During the simulation, we did not specify initial guesses for the magnetic moments and allowed VASP to fully relax the system until the most stable configuration was obtained. All models were visualized using VESTA software (*45*).

Fabrication of flexible Zn-MnO_2 batteries

Cathode slurry was coated onto 0.2-mm stainless steel foil using roll-to-roll equipment, achieving cathode sheets with an active material (MnO_2) loading of ~20 mg cm^{-2}. These sheets and 0.1-mm zinc foil were laser cut into stackable geometries using a three-axis ultraviolet laser system (MD-U1000C, Keyence). Mechanically polished nickel foil (0.2 mm thick, 6 mm wide) served as the interconnect between Zn and MnO_2 electrodes for series connection. The electrolyte solution contained 1 M $ZnSO_4$, 0.3 M $MnSO_4$, and 0.05 M H_2SO_4.

Each flexible battery comprised two electrochemical cells in mirror-symmetric configuration relative to the central axis (fig. S13), effectively reducing mechanical strain and resistance during bending. Separators were laser cut to match electrode geometry and prewetted with 25 μl of electrolyte. The battery components were stacked together, and the resulting multilayer structure was compressed and secured with heat-shrink tubing for intimate contact, then encapsulated in soft silicone elastomer (Ecoflex 00-50) for mechanical robustness and environmental protection (fig. S31 and movie S1).

Fabrication of flexible hybrid circuit

Figure S18 presents the schematic and board layout of the flexible printed circuit board and table S1 lists the bill of materials. Serpentine interconnects electrically connect all components while mechanically dividing the board into two islands to ensure mechanical compliance during wing-flapping motion. Rational placement of the components on the two islands balances the weight distribution for robot stability. A high-precision inertial measurement unit (ICM42688P, InvenSense) sampled at 50 Hz allows real-time attitude detection and motion tracking, and a BLE system-on-chip (nRF52832, Nordic Semiconductor) acquires sensor data and wirelessly transmits to the host computer.

Fabrication of ferromagnetic soft actuator and integrated robot

The fabrication of ferromagnetic elastomer involved mixing silicone (Ecoflex 00-30, Smooth-On) with 5-μm NdFeB particles (MQP-15-7, Magnequench) with a weight ratio of 1:1, casting in 3D-printed PLA molds with the size of 30 mm by 20 mm by 2.5 mm (length × width × thickness), and curing for 2 hours at 60°C. Multiaxial magnetization was implemented on the elastomer through a two-step process. Cosinusoidal magnetization patterns were achieved by wrapping the cured elastomer around a 7-mm-radius tube and applying a 2.70-T pulse magnetic field (IM-10-30, ASC Scientific; fig. S15). Axial magnetization was accomplished through directional alignment between the elastomer and a 0.54-T magnetic field. The magnetized elastomer was then integrated with a laser-cut PMMA skeleton (1 mm thickness) and PET wings (0.3 mm thickness) positioned directly above using 2-mm-thick pure silicone (Fig. 1B). A compartment (22 mm by 12 mm by 2 mm) was incorporated above the robot body to accommodate the battery and circuit assembly using photo-cured soft adhesive (D-0082, Zhuolide).

Battery performance under vibration

To simulate operational conditions of the manta ray soft robot (Fig. 3A), we evaluated battery stability under mechanical vibration using a ZD/LX-XTP-VT700 test system (Huayi Technology). Flexible Zn-MnO_2 batteries were encapsulated in silicone (00-50, Smooth-On) and mounted on either magnetized magnetic elastomer or unmagnetized silicone elastomer (control). Electrochemical performance was evaluated through cyclic voltammetry measurements using an electrochemical workstation (CHI760E, CH Instruments) under sinusoidal waveform (30 Hz fixed frequency, 5 mm amplitude) to evaluate battery behavior under dynamic loading conditions.

Mechanical characterization of integrated robot

Deformation behavior of the manta ray soft robots was characterized through three-point bending tests using a universal testing machine (E42.503, MTC Corp.) equipped with a 50-N force sensor. Tests were conducted under displacement-controlled conditions at 0.1 mm/s loading speed up to 4 mm maximum deflection. Sample positioning and stability were maintained using a pneumatic grip controller (FPC2850, MTC Corp.) that regulated the negative pressure applied

to the robot elastomers. Mechanical behavior was simulated using finite element analysis (COMSOL Multiphysics).

Robot actuation via mobile coil system

The mobile coil system (Fig. 4A and fig. S24A) consisted of a six-axis robotic arm (UR5e, Universal Robots) equipped with an electromagnetic coil (50 mm diameter, 16 mm height, 10 mm iron core, 304 turns) and 16 stacked permanent magnets (10 mm by 5 mm by 2 mm each). All components were mounted via a 3D-printed bracket. The position and orientation of the mobile coil are controlled via manipulation of the robotic arm, allowing free movement within its operational workspace (the hemispherical volume with a radius of 850 mm). Coil's current activation is achieved using a programmable waveform generator (FY8300, Feel Elec) in combination with a power amplifier (GL2530, Paisheng), enabling the generation of a 2-A and 30-Hz alternating current. This induces bending and water-splashing motions in the robot when positioned 30 mm away from the coil by the field of ~10 mT. Besides, the field of permanent magnets applies a magnetic attraction force to the robot, and enables it to move and steer on the water surface in response to the robotic arm movement, thus allowing the execution of complex maneuvers in narrow pipeline environments.

Robot actuation via the electromagnet array

The electromagnet array (Fig. 4D and fig. S24B) comprised 33 electromagnetic coils (35 mm diameter, 20 mm height, 9 mm iron core, 432 turns) arranged in an equilateral triangle configuration with 36.8 mm sides, creating an effective workspace of 220.8 mm by 162.5 mm. The system integrated five coil selectors, each with a maximum of eight channels, to connect coils to current drive circuits and steady voltage sources (RQ-125D, Mean Well) for independent activation control of all coils. An H-bridge circuit configuration with four transistors (IRF3205PBF, Infineon Technologies) serving as bridge arm switches was implemented. Switches' control was achieved through high-frequency complementary pulse width modulation (PWM) signals from a microcontroller (STM32F767ZIT6, STMicroelectronics). By modulating the voltage polarity and duration through PWM signals while maintaining the constant source voltage, a single coil's activating current magnitude exhibited a linear relationship with PWM duty ratio. Sequential activation of neighboring coils results in a spatially shifting magnetic field, which guides the ferromagnetic robot positioned above the coil array to execute locomotion along a predefined trajectory.

Servo motion of magnetic actuation

Axial magnetization along the x axis imparts directionality to the robot by forming the magnetic dipole between the robot's head and tail, enabling it to be captured by the spatial field with the magnetic dipole distribution generated by the coil system. This enables the robot to remain stably within the coil's magnetic field area and grants it a certain degree of resistance to light disturbances on the water surface (movie S11). When the robot is captured by the coil-generated field, its locomotion under magnetic actuation exhibits a nearly constant acceleration along the x axis, and its yaw orientation continues to align with the horizontal direction of the generated spatial magnetic field. Therefore, fluctuations in acceleration and deviations in the yaw angle can be used to infer collisions with obstacles during motion or indicate external disturbances, thereby triggering corresponding avoidance or correction protocols.

Supplementary Materials

The PDF file includes:

Supplementary Text S1 and S2
Figs. S1 to S32
Table S1
Legend for movies S1 to S14
References

Other Supplementary Material for this manuscript includes the following:

Movies S1 to S14

REFERENCES AND NOTES

1. M. H. Dickinson, C. T. Farley, R. J. Full, M. A. R. Koehl, R. Kram, S. Lehman, How animals move: An integrative view. *Science* **288**, 100–106 (2000).
2. S. A. Burden, T. Libby, K. Jayaram, S. Sponberg, J. M. Donelan, Why animals can outrun robots. *Sci. Robot.* **9**, eadi9754 (2024).
3. P. Ramdya, A. J. Ijspeert, The neuromechanics of animal locomotion: From biology to robotics and back. *Sci. Robot.* **8**, eadg0279 (2023).
4. G. Z. Yang, J. Bellingham, P. E. Dupont, P. Fischer, L. Floridi, R. Full, N. Jacobstein, V. Kumar, M. McNutt, R. Merrifield, B. J. Nelson, B. Scassellati, M. Taddeo, R. Taylor, M. Veloso, Z. L. Wang, R. Wood, The grand challenges of *Science Robotics*. *Sci. Robot.* **3**, eaar7650 (2018).
5. C. A. Aubin, B. Gorissen, E. Milana, P. R. Buskohl, N. Lazarus, G. A. Slipher, C. Keplinger, J. Bongard, F. Iida, J. A. Lewis, R. F. Shepherd, Towards enduring autonomous robots via embodied energy. *Nature* **602**, 393–402 (2022).
6. V. G. Kortman, B. Mazzolai, A. Sakes, J. Jovanova, Perspectives on intelligence in soft robotics. *Adv. Intell. Syst.* **7**, (2025).
7. M. Wang, D. Vecchio, C. Wang, A. Emre, X. Xiao, Z. Jiang, P. Bogdan, Y. Huang, N. A. Kotov, Biomorphic structural batteries for robotics. *Sci. Robot.* **5**, eaba1912 (2020).
8. Z. Wang, Q. Zhao, X. Yu, W. An, B. Shi, Impacts of vibration and cycling on electrochemical characteristics of batteries. *J. Power Sources* **601**, 234274 (2024).
9. M. H. Kim, S. Nam, M. Oh, H. J. Lee, B. Jang, S. Hyun, Bioinspired, shape-morphing scale battery for untethered soft robots. *Soft Robot.* **9**, 486–496 (2022).
10. C. A. Aubin, S. Choudhury, R. Jerch, L. A. Archer, J. H. Pikul, R. F. Shepherd, Electrolytic vascular systems for energy-dense robots. *Nature* **571**, 51–57 (2019).
11. N. W. Bartlett, M. T. Tolley, J. T. B. Overvelde, J. C. Weaver, B. Mosadegh, K. Bertoldi, G. M. Whitesides, R. J. Wood, A 3D-printed, functionally graded soft robot powered by combustion. *Science* **349**, 161–165 (2015).
12. X. Liu, S. Jin, Y. Shao, S. Kuperman, A. Pratt, D. Zhang, J. Lo, Y. L. Joo, A. D. Gat, L. A. Archer, R. F. Shepherd, The multifunctional use of an aqueous battery for a high capacity jellyfish robot. *Sci. Adv.* **10**, eadq7430 (2024).
13. X. Lai, C. Jin, W. Yi, X. Han, X. Feng, Y. Zheng, M. Ouyang, Mechanism, modeling, detection, and prevention of the internal short circuit in lithium-ion batteries: Recent advances and perspectives. *Energy Storage Mater* **35**, 470–499 (2021).
14. S. Wu, Y. Chen, W. Luan, H. Chen, L. Huo, M. Wang, S. Tu, A review of multiscale mechanical failures in lithium-ion batteries: Implications for performance, lifetime and safety. *Electrochem. Energy Rev.* **7**, 35 (2024).
15. J. Byun, Y. Lee, J. Yoon, B. Lee, E. Oh, S. Chung, T. Lee, K.-J. Cho, J. Kim, Y. Hong, Electronic skins for soft, compact, reversible assembly of wirelessly activated fully soft robots. *Sci. Robot.* **3**, eaas9020 (2018).
16. S. I. Rich, R. J. Wood, C. Majidi, Untethered soft robotics. *Nat. Electron.* **1**, 102–112 (2018).
17. Z. Ren, R. Zhang, R. H. Soon, Z. Liu, W. Hu, P. R. Onck, M. Sitti, Soft-bodied adaptive multimodal locomotion strategies in fluid-filled confined spaces. *Sci. Adv.* **7**, eabh2022 (2021).
18. R. Dreyfus, Q. Boehler, S. Lyttle, P. Gruber, J. Lussi, C. Chautems, S. Gervasoni, J. Berberat, D. Seibold, N. Ochsenbein-Kölble, M. Reinehr, M. Weisskopf, L. Remonda, B. J. Nelson, Dexterous helical magnetic robot for improved endovascular access. *Sci. Robot.* **9**, eadh0298 (2024).
19. Y. Kim, E. Genevriere, P. Harker, J. Choe, M. Balicki, R. W. Regenhardt, J. E. Vranic, A. A. Dmytriw, A. B. Patel, X. Zhao, Telerobotic neurovascular interventions with magnetic manipulation. *Sci. Robot.* **7**, eabg9907 (2022).
20. Y. Kim, G. A. Parada, S. Liu, X. Zhao, Ferromagnetic soft continuum robots. *Sci. Robot.* **4**, eaax7329 (2019).
21. Y. Dong, L. Wang, N. Xia, Z. Yang, C. Zhang, C. Pan, D. Jin, J. Zhang, C. Majidi, L. Zhang, Untethered small-scale magnetic soft robot with programmable magnetization and integrated multifunctional modules. *Sci. Adv.* **8**, eabn8932 (2022).
22. B. Oh, Y. G. Park, H. Jung, S. Ji, W. H. Cheong, J. Cheon, W. Lee, J. U. Park, Untethered soft robotics with fully integrated wireless sensing and actuating systems for somatosensory and respiratory functions. *Soft Robot.* **7**, 564–573 (2020).
23. O. Aaboubi, J. P. Chopart, J. Douglade, A. Olivier, C. Gabrielli, B. Tribollet, Magnetic field effects on mass transport. *J. Electrochem. Soc.* **137**, 1796–1804 (1990).

24. P. Vensaus, Y. Liang, J. P. Ansermet, G. J. A. A. Soler-Illia, M. Lingenfelder, Enhancement of electrocatalysis through magnetic field effects on mass transport. *Nat. Commun.* **15**, 2867 (2024).
25. A. Wang, Q. Deng, L. Deng, X. Guan, J. Luo, Eliminating tip dendrite growth by Lorentz force for stable lithium metal anodes. *Adv. Funct. Mater.* **29**, 1902630 (2019).
26. K. Shen, Z. Wang, X. Bi, Y. Ying, D. Zhang, C. Jin, G. Hou, H. Cao, L. Wu, G. Zheng, Y. Tang, X. Tao, J. Lu, Magnetic field–suppressed lithium dendrite growth for stable lithium-metal batteries. *Adv. Energy Mater.* **9**, 1900260 (2019).
27. X. Wang, S. Zheng, F. Zhou, J. Qin, X. Shi, S. Wang, C. Sun, X. Bao, Z.-S. Wu, Scalable fabrication of printed Zn//MnO_2 planar micro-batteries with high volumetric energy density and exceptional safety. *Natl. Sci. Rev.* **7**, 64–72 (2020).
28. D. Chao, W. Zhou, C. Ye, Q. Zhang, Y. Chen, L. Gu, K. Davey, S.-Z. Qiao, An electrolytic Zn-MnO_2 battery for high-voltage and scalable energy storage. *Angew. Chem. Int. Ed.* **58**, 7823–7828 (2019).
29. X. Xiao, Z. Zheng, X. Zhong, R. Gao, Z. Piao, M. Jiao, G. Zhou, Rational design of flexible Zn-based batteries for wearable electronic devices. *ACS Nano* **17**, 1764–1802 (2023).
30. Y. Liang, Y. Yao, Designing modern aqueous batteries. *Nat. Rev. Mater.* **8**, 109–122 (2023).
31. J. S. E. Townsend, The diffusion and mobility of ions in a magnetic field. *Proc. R. Soc. Lond. A* **86**, 571–577 (1912).
32. A. E. D. Heylen, Propagation of a gaseous discharge in a crossed magnetic field. *Nature* **203**, 745 (1964).
33. Y. Yuan, R. Sharpe, K. He, C. Li, M. T. Saray, T. Liu, W. Yao, M. Cheng, H. Jin, S. Wang, K. Amine, R. Shahbazian-Yassar, M. S. Islam, J. Lu, Understanding intercalation chemistry for sustainable aqueous zinc–manganese dioxide batteries. *Nat. Sustain.* **5**, 890–898 (2022).
34. Y. Liu, C. Xie, X. Li, Carbon nanotube network induces porous deposited MnO_2 for high-areal capacity Zn/Mn batteries. *Small* **20**, e2402026 (2024).
35. Z. Hou, J. Wang, N. Dai, S. Yao, S. Wang, Y. Ji, X. Gao, H. Zhang, Z. Tang, Y. Sun, S. Li, Y. Liu, W. Fu, K. Nie, Y. Jiang, Y. Yan, Z. Yang, Eliminating the Mn 3d orbital degeneracy to suppress the Jahn–Teller distortion for stable MnO_2 cathode. *Adv. Energy Mater.* **14**, 2302477 (2024).
36. Y. Jiang, L. Yuan, X. Wang, W. Zhang, J. Liu, X. Wu, K. Huang, Y. Li, Z. Liu, S. Feng, Jahn–Teller disproportionation induced exfoliation of unit-cell scale ϵ-MnO_2. *Angew. Chem. Int. Ed.* **59**, 22659–22666 (2020).
37. D. von Arx, C. Fischer, H. Torlakcik, S. Pané, B. J. Nelson, Q. Boehler, D. von Arx, Simultaneous localization and actuation using electromagnetic navigation systems. *IEEE Trans. Robot.* **40**, 1292–1308 (2024).
38. M. Urso, M. Ussia, F. Novotný, M. Pumera, Trapping and detecting nanoplastics by MXene-derived oxide microrobots. *Nat. Commun.* **13**, 3573 (2022).
39. X. Xiao, X. Xiao, Y. Zhou, X. Zhao, G. Chen, Z. Liu, Z. Wang, C. Lu, M. Hu, A. Nashalian, S. Shen, K. Xie, W. Yang, Y. Gong, W. Ding, P. Servati, C. Han, S. X. Dou, W. Li, J. Chen, An ultrathin rechargeable solid-state zinc ion fiber battery for electronic textiles. *Sci. Adv.* **7**, eabl3742 (2021).
40. G. Kresse, J. Hafner, Ab initio molecular-dynamics simulation of the liquid-metal–amorphous-semiconductor transition in germanium. *Phys. Rev. B* **49**, 14251–14269 (1994).
41. S. L. Dudarev, G. A. Botton, S. Y. Savrasov, C. J. Humphreys, A. P. Sutton, Electron-energy-loss spectra and the structural stability of nickel oxide: An LSDA+U study. *Phys. Rev. B* **57**, 1505–1509 (1998).
42. P. E. Blöchl, Projector augmented-wave method. *Phys. Rev. B* **50**, 17953–17979 (1994).
43. G. Kresse, D. Joubert, From ultrasoft pseudopotentials to the projector augmented-wave method. *Phys. Rev. B* **59**, 1758–1775 (1998).
44. X. Ren, T. Wu, Y. Sun, Y. Li, G. Xian, X. Liu, C. Shen, J. Gracia, H. J. Gao, H. Yang, Z. J. Xu, Spin-polarized oxygen evolution reaction under magnetic field. *Nat. Commun.* **12**, 2608 (2021).
45. K. Momma, F. Izumi, *VESTA 3* for three-dimensional visualization of crystal, volumetric and morphology data. *J. Appl. Cryst.* **44**, 1272–1276 (2011).
46. S. H. Kim, K. Shin, S. Hashi, K. Ishiyama, Magnetic fish-robot based on multi-motion control of a flexible magnetic actuator. *Bioinspir. Biomim.* **7**, 036007 (2012).
47. L. Tsai, A numerical solution for the near and far fields of an annular ring of magnetic current. *IEEE Trans. Antennas Propag.* **20**, 569–576 (1972).
48. A. Sarwar, A. Nemirovski, B. Shapiro, Optimal Halbach permanent magnet designs for maximally pulling and pushing nanoparticles. *J. Magn. Magn. Mater.* **324**, 742–754 (2012).
49. X. Li, C. Lu, Z. Song, W. Ding, X.-P. Zhang, Planar magnetic actuation for soft and rigid robots using a scalable electromagnet array. *IEEE Robot. Autom. Lett.* **7**, 9264–9270 (2022).

Acknowledgments: We acknowledge J. Trueb, Z. Liu, X. Li, and J. Xiao for their insightful discussions and help. **Funding:** X.L. and W.D. acknowledge the support from the Shenzhen Key Laboratory of Ubiquitous Data Enabling (no. ZDSYS20220527171406015), the Shenzhen Science and Technology Program (JCYJ20220530143013030), the Guangdong Innovative and Entrepreneurial Research Team Program (2021ZT09L197), the National Natural Science Foundation of China (62104125), and the Tsinghua Shenzhen International Graduate School-Shenzhen Pengrui Young Faculty Program of Shenzhen Pengrui Foundation (no. SZPR2023005). X.X. (second author), W.D., and G.Z. acknowledge the support from the Guangdong Innovative and Entrepreneurial Research Team Program (2021ZT09L197), Guangdong Basic and Applied Basic Research Foundation (2023B1515120099), the Shenzhen Science and Technology Program (KQTD20210811090112002), and the Joint Funds of the National Natural Science Foundation of China (U21A20174). X.X. (third author), J.S.H., P.C., and C.W. acknowledges the support and funding from the National Research Foundation, Singapore, and A*STAR under its RIE2020 Industry Alignment Fund-Industry Collaboration Projects (IAF-ICP) grant call (grant no. I2001E0059). C.W. acknowledges support and funding from the National University of Singapore Presidential Young Professorship Start Up Grant. C.L. acknowledges the support from the NUS start-up grant RoboLife (A-0009125-02-00).
Author contributions: Conceptualization: X.L., X.X. (second author), X.X. (third author), W.D., G.Z., and C.W. Methodology: X.L., X.X. (second author), X.X. (third author), W.O., W.D., G.Z., and C.W. Investigation: X.L., X.X. (second author), X.X. (third author), Z. Liu, J.G., Z. Lin, B.X., S.L., X.W., W.D., G.Z., and C.W. Visualization: X.L., X.X. (second author), X.X. (third author), W.D., and C.W. Supervision: W.D., G.Z., and C.W. Writing—original draft: X.L., X.X. (second author), X.X. (third author), and C.W. Writing—review and editing: all authors **Competing interests:** The authors declare that they have no competing interests. **Data and materials availability:** All data needed to evaluate the conclusions in the paper are present in the paper and/or the Supplementary Materials.

Submitted 13 January 2025
Accepted 8 August 2025
Published 10 September 2025
10.1126/sciadv.adv9572